



Numerical Tool for Calculating Birefringence in Mirror-Substrates for Gravitational-Wave Detectors

Simon Zeidler*

Murata-laboratory, Department of Physics, Rikkyo University, Toshima-City, Japan

The influence of birefringence on rays entering and exiting a non-isotropic medium is a complex process that depends on its dielectric tensor, the orientation and geometry of the medium, the surrounding material, and the inclination of the incident ray. Thus, when aiming for a calculation of the effects, many parameters need to be taken into account while simplifications are generally not applicable. Moreover, the complexity of the general issue makes it almost impossible to find an analytical solution for backward calculations of stress-birefringence from polarization measurements. In this paper, a report is given on the formulation of a birefringence ray-tracing program in Python for the convenient evaluation of optical effects inside uniaxial crystals under stress. The aim thereby is to have an easily applicable tool that can be used in interferometer commissioning for current and future gravitational-wave detectors. Results from test simulations using realistic parameters for a sapphire mirror as used in the gravitational-wave detector KAGRA are implemented and show the capabilities of this tool.

Keywords: numerical analysis, gravitational-wave detector, sapphire, birefringence, optic

OPEN ACCESS

Edited by:

Matteo Montani,
University of Urbino Carlo Bo, Italy

Reviewed by:

Jonathan W. Arenberg,
Northrop Grumman, United States
Mihai Bondarescu,
University of Mississippi, United States

*Correspondence:

Simon Zeidler
s.zeidler@rikkyo.ac.jp

Specialty section:

This article was submitted to
High-Energy and Astroparticle
Physics,
a section of the journal
Frontiers in Astronomy and Space
Sciences

Received: 22 February 2022

Accepted: 05 May 2022

Published: 23 June 2022

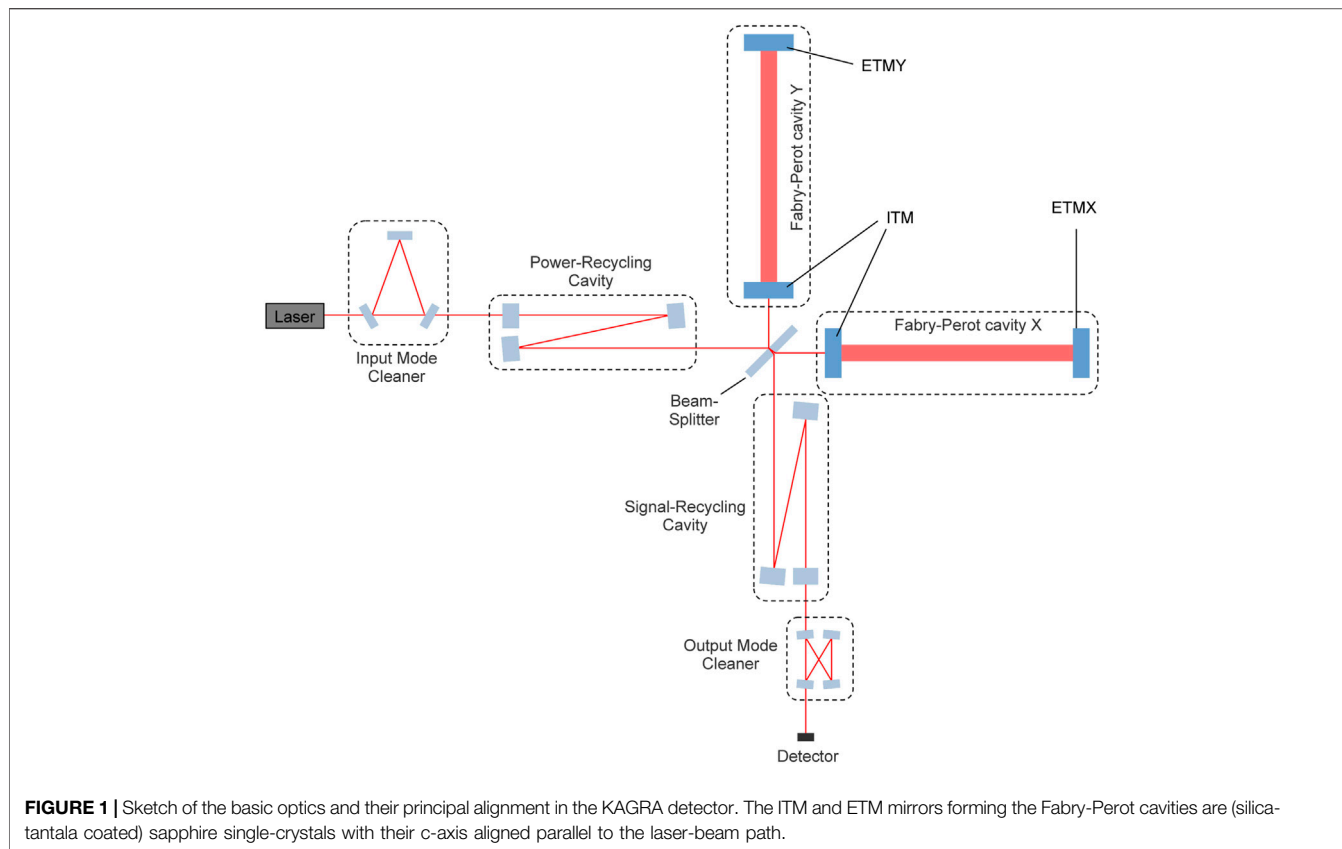
Citation:

Zeidler S (2022) Numerical Tool for
Calculating Birefringence in Mirror-
Substrates for Gravitational-
Wave Detectors.
Front. Astron. Space Sci. 9:881348.
doi: 10.3389/fspas.2022.881348

1 INTRODUCTION

Large-scale laser-interferometer form the fundamental technology of modern gravitational-wave detectors like LIGO in the United States (Aasi et al. (2015)), Virgo in Italy (Acernese et al. (2015)) and KAGRA in Japan (Akutsu et al. (2019; 2020)). This technology proved to be successful in the detection of gravitational waves (Abbott et al. (2016)). Ever since, the number of detections is rising and while the observations give enormous insight into previously only theoretically describable phenomena, scientists are striving to further upgrade the existing detectors to increase their sensitivity and broaden the detectable frequency range (Kalogera et al. (2021); Bailes et al. (2021)). Newer detectors like KAGRA entered the stage of gravitational-wave detection at lower sensitivities and still have to catch up to the current limits, mainly set by the LIGO detectors (Akutsu et al. (2020); Martynov et al. (2016); Aso et al. (2013)). KAGRA, in particular, is using cryogenic cooled mirrors which decreases the thermal noise limiting sensitivity at higher frequencies to a greater extent than LIGO and Virgo can do with room-temperature mirrors (Akutsu et al. (2020)).

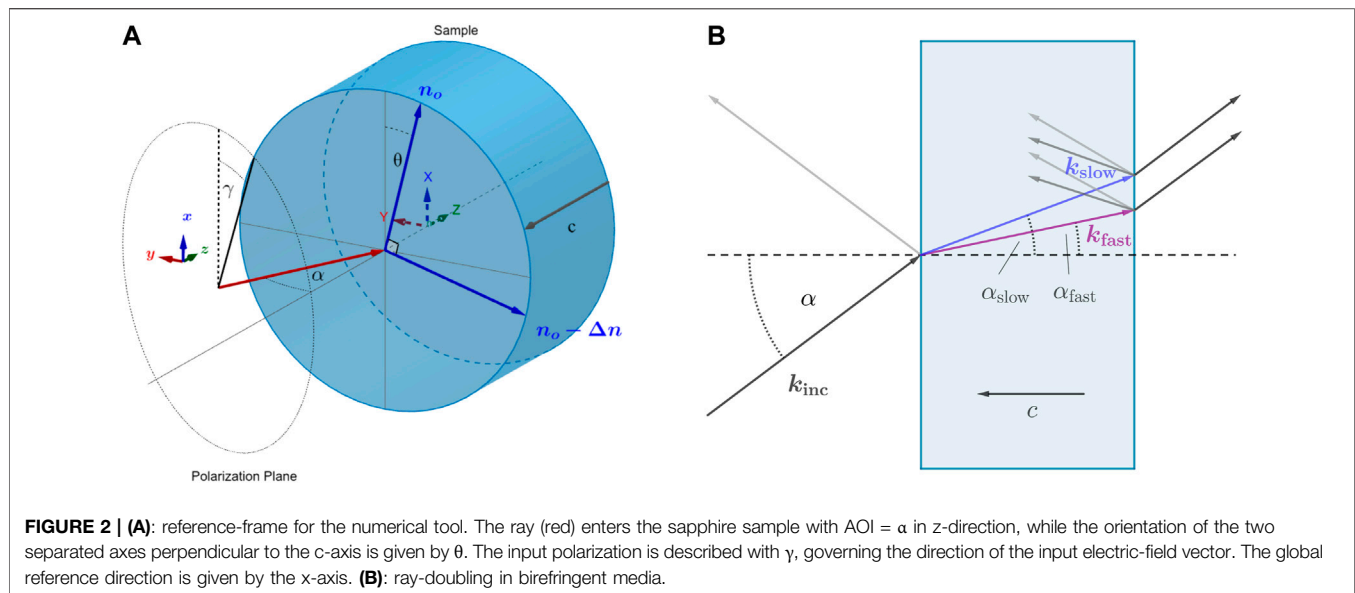
Unsurprisingly, the most sensitive parts of those detectors are their optics. The most crucial components are formed by the large (and heavy) mirrors that create the Fabry-Perot cavities (“test-mass”, or TM). In each cavity a large amount of laser-energy is stored which increases the effective sensitivity to space-time deformations of gravitational waves (Saulson (1994)). The partially transmitting mirror at the beam-splitter side of the cavities (ITM) thereby governs the properties of the light entering and exiting (see also **Figure 1** for a basic outline of the optics alignment in KAGRA). Since all mirror-coatings in those detectors are designed to reflect (or



transmit) a specific portion of light depending on the polarization, it is of utmost importance for the signal's readout that the polarization remains constant inside the interferometer. A change of polarization especially at the ITMs will decrease the effective signal-power and thus harm sensitivity. While in reflection the dependence of polarization on external parameters like the angle of incidence (AOI) can be kept low by accurately engineered coatings, in transmission a lot more uncertainties exist which make it difficult to predict the precise behavior of the transmitted polarization. Polarization characterization by polariscopes could be very helpful but are still not a standard technique in the construction of gravitational-wave detectors. Instead, transmitted wavefront-error (TWE) maps are analyzed which can indeed detect local density inhomogeneities and thus changes of the refraction index. This however only if the changes are isotropic (Chipman et al. (2018)). For anisotropic inhomogeneities of the refraction index, TWE maps taken at different rotation angles need to be taken and analyzed, an endeavor which currently just has started. In KAGRA the substrate of ITMs is made of sapphire, a non-isotropic (uniaxial) crystal which naturally can change the input polarization of an incoming beam if it is not aligned to be parallel to the sapphire's c-axis (Dobrovinskaya et al. (2009)). Small inhomogeneities during the growth of the crystal can lead to local misalignment (crystal-defect) and hence disturbed polarization performance. LIGO and Virgo, on the other side, are using substrates made of silica (amorphous SiO_2) for their

test-masses which is isotropic. But even though, internal stress remaining from manufacturing can turn isotropic materials into (locally) uniaxial ones, making them to behave basically as an anisotropic waveplate (Chipman et al. (2018)). Uniaxial crystals on the other hand may become even biaxial if internal stress resides.

In general, when an electromagnetic plane-wave enters an uniaxial or biaxial material, it will split into two separate fields representing its eigenpolarizations inside the material and traveling in different directions (see Figure 2). Polarization direction, wavevector \mathbf{k} and Poynting vector \mathbf{S} of each eigenstate are a function of the material's indicatrix (refraction-index ellipsoid), AOI, and incoming medium's optical properties (since in this paper the case of gravitational-wave interferometer is treated, the incoming medium will be assumed to be a vacuum and therefore isotropic). Usually, it is just a mirror's coating that is of concern when designing its properties which is to reflect and transmit a particular portion of incoming light under a given constraint. Hence, the thickness of mirror-substrates may be of not great interest and can become even negligible for light passing it if birefringence is sufficiently small. In gravitational-wave detectors, however, the test-masses need to meet certain mass and geometry requirements in order to fulfill suspension constraints (Saulson (1994)) or (in case of KAGRA) constraints on thermal conductivity (Akutsu et al. (2020)). The substrates of ITMs are therefore particularly thick. For example, the test-masses in KAGRA measure



220 mm in diameter and ~ 150 mm in thickness (given are the mean values). With such thicknesses even small AOIs lead to considerable optical path differences between the two refracted beams and thus to changes in the resulting polarization once the beams emerge from the sample. Here, we assume a typical laser-beam ($\lambda = 1064$ nm with $\phi = 35$ mm after Aso et al. (2014)) entering the ITMs in KAGRA. The change in polarization is thereby a result of both beams overlapping each other when leaving the substrate. Moreover, even when normal incidence is assured, small changes in the orientation of the indicatrix will also lead to ray-doubling and hence polarization changes. On the other side, any Gaussian beam offers a constantly changing AOI throughout its wavefront when impacting a mirror, thus ray-doubling appears as a function of the wavefront curvature leading to multiple beams passing the substrate. Understanding how the polarization of laser-beams is altered when transmitting through TMs is thus an important aspect in the selection of substrates as well as the calibration of gravitational-wave detectors and should be taken seriously into account for any future detector striving to even greater sensitivities.

In this paper, a tool will be presented to calculate the impact of internal-stress and changes in indicatrix-orientation on the polarization of rays passing large mirror-substrates using the NumPy and SymPy packages in Python. The theoretical concept of this tool is based on the chapters 10, 19 and 21 of the book “Polarized Light and Optical Systems” by Chipman et al. (2018) where the algorithm is explained in much greater detail. In **Section 2**, I will thus first give a brief overview of the calculus before the specific case of sapphire substrates in KAGRA is discussed. In **Section 3**, then, I will present calculation results using the ray-tracing tool from **Section 2** to show dependencies of the polarization-impact on stress-induced birefringence and indicatrix alignment for the sapphire substrate as used by KAGRA. Possible impacts of the polarization changes on the sensitivity in gravitational-wave detectors and ray-doubling in KAGRA ITMs will be discussed in **Section 4**.

2 THEORETICAL CONCEPT OF POLARIZATION RAY-TRACING

In an uniaxial crystal like sapphire, we usually distinguish between an optical axis, denoted as extraordinary, or e , and ordinary axes, o , perpendicular to e . Along e , we find a different refraction index than for o which can be larger (*positive* crystal) or smaller (*negative* crystal). If we introduce a stress-tensor affecting the crystal, then generally we have to assume that among axes in o a splitting of the refraction index appears, changing the uniaxial crystal to become basically a biaxial crystal with three refraction indexes along three independent directions. However, unlike pure biaxial crystals, the generation of refraction indexes becomes a function of the spatial vector \mathbf{r} , due to the spatial distribution of stress. Hence, each point of the crystal under stress has its own unique indicatrix and needs to be treated individually. This is why a simplification of the problem cannot be done. Moreover, since the representation of the crystal changes to be biaxial, we distinguish a *fast* and a *slow* axis for each beam entering the crystal where the electric field experiences a refraction index which is either smaller or larger.

Each separate beam along the fast and along the slow axis represent the electric field’s eigenstate inside the crystal. An important aspect for polarization ray-tracing is therefore a proper description of the electric-field vector \mathbf{E} since it defines the direction of polarization. In the general case, the field along the fast axis \mathbf{E}_{fast} and the field along the slow axis \mathbf{E}_{slow} have different directions and need thus to be treated separately. As we are using a very general description in global coordinates, a utilization of Jones-vectors and matrices is not very effective and a more generalized calculus in three dimensions with, so called, \mathbf{P} -matrices is applied (Chipman et al. (2018)). A \mathbf{P} -matrix relates an incoming electric field with its outgoing counterpart of any system in the form

$$\mathbf{E}_{\text{out}} = \mathbf{P} \cdot \mathbf{E}_{\text{inc}}. \tag{1}$$

Each beam emerging from a system has its own P-matrix where all information about the emerging field are encoded in, inclusively transmission and reflection ratios. In the following, I will show how to construct a P-matrix in a general way before a description of biaxial systems with the presented calculus will be done.

2.1 Constructing P-Matrices

A very comprehensive description of how a P-matrix is derived for various cases can be found in the mentioned book by Chipman et al. (2018). Here, I will just give a brief overview of the construction.

When a plane-wave reaches an interface between two media, we can generally expect a splitting into 4 different waves: two in transmission and two in reflection. Each of them traveling in a different direction as they experience their own index of refraction. It is thus the refraction index n which firstly needs to be calculated for each refracted/reflected wave. On the other side, n appears as a function of \mathbf{k} for each wave and vice versa. Thus, both parameter have to be derived simultaneously. From Maxwell's equations, it is straightforward to show that in any medium

$$\mathbf{k} \times (\mathbf{k} \times \mathbf{E}) + \frac{\omega^2}{c^2} \boldsymbol{\varepsilon} \mathbf{E} = 0, \tag{2}$$

where ω is the angular frequency of the wave and c the speed of light in vacuum. The dielectric tensor $\boldsymbol{\varepsilon}$, which relates the variation in refractive index with the polarization direction of the electric field inside a medium, can be written as (using local coordinates X,Y,Z)

$$\boldsymbol{\varepsilon} = \begin{pmatrix} \varepsilon_X & 0 & 0 \\ 0 & \varepsilon_Y & 0 \\ 0 & 0 & \varepsilon_Z \end{pmatrix} = \begin{pmatrix} (n_X + i\kappa_X)^2 & 0 & 0 \\ 0 & (n_Y + i\kappa_Y)^2 & 0 \\ 0 & 0 & (n_Z + i\kappa_Z)^2 \end{pmatrix}, \tag{3}$$

with κ as the absorption index. Please refer to **Figure 2** for a description of the reference frame. In **Eq. 2**, the influence of magnetic permeability has been omitted as it will not be of any concern for the issues to be discussed. We can further simplify **Eq. 2** to

$$(\boldsymbol{\varepsilon} + n^2 \mathbf{K}^2) \mathbf{E} = 0, \quad \text{with} \quad \mathbf{K} = \begin{pmatrix} 0 & -\hat{k}_z & \hat{k}_y \\ \hat{k}_z & 0 & -\hat{k}_x \\ -\hat{k}_y & \hat{k}_x & 0 \end{pmatrix}, \tag{4}$$

with the normalized vector $\hat{\mathbf{k}}$.

Consider now an intercept between two media 1 and 2, whereas we know the input wavevector \mathbf{k}_1 and refractive index n_1 . In order to find solutions for \mathbf{k}_2 and n_2 one can use the generalized Snell's law:

$$\mathbf{k}_1 \times \mathbf{N} = \mathbf{k}_2 \times \mathbf{N}, \tag{5}$$

and the assumption that any \mathbf{k}_2 can be constructed from the normalized vectors $\hat{\mathbf{k}}_1$ and $\hat{\mathbf{N}}$ (\mathbf{N} being the intercept's normal) as basis vectors. The expression in **Eq. 5** is also valid for reflected

rays. By setting the determinant of the matrix in **Eq. 4** for the waves in medium 2 zero, the necessary set of equations which need to be solved is given by

$$\hat{\mathbf{k}}_2 = \frac{n_0 \hat{\mathbf{k}}_1 + \left(-n_0 \hat{\mathbf{k}}_1 \cdot \hat{\mathbf{N}} + \sqrt{n_2^2 - n_1^2 + n_1^2 \hat{\mathbf{k}}_1 \cdot \hat{\mathbf{N}}} \right) \cdot \hat{\mathbf{N}}}{\left| n_1 \hat{\mathbf{k}}_1 + \left(-n_1 \hat{\mathbf{k}}_1 \cdot \hat{\mathbf{N}} + \sqrt{n_2^2 - n_1^2 + n_1^2 \hat{\mathbf{k}}_1 \cdot \hat{\mathbf{N}}} \right) \cdot \hat{\mathbf{N}} \right|} \tag{6}$$

$$|\boldsymbol{\varepsilon} + n_2^2 \mathbf{K}_2^2| = 0.$$

Once wavevectors and refraction indexes are known, the field vectors of both electric and magnetic field are calculated for slow and fast wave in refraction and reflection. By singular-value decomposition of the matrix-part in **Eq. 4**, one will then get the electric fields. The P-matrices, finally, can then be calculated by using the field- and Poynting-vectors of the incoming beam together with the transmission and reflection coefficients of each eigenstate ("1" and "2") of the incoming field. In the following the coefficients are summarized into vectors, referring to them as \mathbf{t}_1 , and \mathbf{t}_2 . For a more detailed description how to calculate the coefficient matrices, see the **Supplementary Appendix**. Using $i = (\text{tf, ts, rf, rs})$ as index for each transmitted fast/slow ray (tf, ts) or reflected fast/slow ray (rf, rs), we can write (Chipman et al. (2018))

$$\mathbf{P}_i = \left(t_{i,1} \cdot \hat{\mathbf{E}}_i \quad t_{i,2} \cdot \hat{\mathbf{E}}_i \quad \hat{\mathbf{S}}_i \right) \cdot \left(\hat{\mathbf{E}}_{\text{inc},1} \quad \hat{\mathbf{E}}_{\text{inc},2} \quad \hat{\mathbf{S}}_{\text{inc}} \right)^T. \tag{7}$$

By changing into global coordinates, the $\boldsymbol{\varepsilon}$ -tensor needs to be rotated accordingly, but the general calculation scheme will not change.

2.2 Describing Stress-Induced Uniaxial Crystals

With the P-matrices at hand, we can describe a ray passing any medium of concern. The objective is, however, to do so in stress-induced media, and particular in sapphire. Sapphire is a variety of crystalline Al_2O_3 which crystallizes in a hexagonal lattice-structure. The oxygen anions are arranged in a (slightly distorted) hexagonal close-packing in which the aluminum cations occupy two thirds of the octahedral interstices (Zeidler et al. (2013); Dobrovinskaya et al. (2009)). Due to this, we can differentiate between a distinct axis along the hexagon (c-axis) and 3 axes perpendicular to the c-axis representing the 3 symmetry-directions of a hexagon's barrel. In the following, we will consider that the sapphire is characterized by a spatially modulated birefringence perturbation superimposed to the constant intrinsic birefringence of the crystal which is given by $n_o - n_e = 0.008$, with $n_o \approx 1.754$ and $n_e \approx 1.746$ (Harris et al. (2017)), the refractive indexes of sapphire at 1064 nm wavelength.

Sapphire, as well as fused silica, are manufactured by cooling down a melt. During the cooling process, naturally temperature gradients within the material appear which lead to stress that is preserved in the material when it crystallizes (or solidifies). According to Dobrovinskaya et al. (2009), the typical amount of stress inside a sapphire bulk may range from 1 to 90 MPa (σ_{min} and σ_{max}), depending on the manufacturing process and whether

or not annealing has been applied. In the given case of sapphire substrates for test-masses in KAGRA, the constraints on refraction index homogeneity are quite strict. Hence, I will assume an amount of residual stress with a mean $\bar{\sigma} = 1 \pm 0.5\text{MPa}$ which would be consistent with the distribution of stress inside samples annealed at temperature well above 2300K (Dobrovinskaya et al. (2009)). As noted above, stress applied to the sample, which is usually described in form of a tensor σ , affects the indicatrix of the anisotropic optical system. The (material specific) coefficients which determine the change of the indicatrix are in turn given by a fourth-rank elasto-optic tensor (Nye (1985)).

The components of this tensor are known in case of sapphire (Bradley (1963)) and by using the model of a deformed indicatrix which is projected on a plane, the following relation can be obtained (see also Iwaki and Koizumi (1989)):

$$\begin{aligned} (\sigma_1 - \sigma_2) + 2\sigma_4 \cdot \frac{p_{14}}{p_{11} - p_{12}} &= \sigma_{\parallel} = \frac{2\Delta n}{n_o^3(p_{11} - p_{12})} \cdot \cos(2\theta) \\ \sigma_6 + \sigma_5 \cdot \frac{p_{14}}{p_{11} - p_{12}} &= \sigma_{\perp} = \frac{4\Delta n}{n_o^3(p_{11} - p_{12})} \cdot \sin(2\theta), \end{aligned} \tag{8}$$

where we have used an eigenvalue decomposition of the projected indicatrix and the reasonable assumption that the stress-induced birefringence is weak ($\Delta n \ll |n_o - n_e|$). Using the assumed distribution of the stress-tensor's coefficients, we can derive an expectation of Δn to be $\sim 2.8 \cdot 10^{-6}$. Setting Z to be the local direction of the c-axis and omitting any absorption, we can express ϵ from Eq. 3 for a stress-induced sapphire as

$$\epsilon = \begin{pmatrix} n_o^2 & 0 & 0 \\ 0 & (n_o - \Delta n)^2 & 0 \\ 0 & 0 & n_e^2 \end{pmatrix}. \tag{9}$$

Without limiting generality, the (additional) birefringence Δn affects the middle component of ϵ only. As Δn is assumed small, the resulting polarization of a ray passing a medium with an ϵ -tensor as given in Eq. 9 will not change if the left component becomes $(n_o + \Delta n)^2$. In this view, n_e is assumed to be constant which cannot be guaranteed in general. A change, however, will only negligibly affect the passing beam since α is assumed to be small.

2.3 Numerical Implementation of the Code

The above given mathematics of polarization ray-tracing are relatively straightforward. Their implementation into a numerical code, however, can become quite complex, particularly if both refracted and reflected rays are to be tracked. The code that has been written for the here given problem uses the reference-frame as illustrated in Figure 2 and is accessible on GitHub (<https://github.com/Zeidler-Akiyama/Birefringence>). A ray entering the substrate is first described in global coordinates by its wavevector \mathbf{k}_{inc} and its electric-field vector \mathbf{E}_{inc} having a linear polarization. From the given ϵ -tensors for both substrate and incoming medium (again in global coordinates), \mathbf{k}_{inc} , and the intercept's normal N , the refraction indexes for transmission and reflection are calculated using SymPy's symbolic algebra system. Since the incoming

medium is a vacuum, the index of refraction for the reflected ray does not need to be calculated this way. However, the algorithm is written with a general application in mind and will produce results for the reflected ray if desired. At the same time, the symbolic calculation procedure is the most time-consuming part, particularly when using SymPy's "solve" algorithm with cross-checking enabled. Thus, if not explicitly needed, the calculation of the reflection should be omitted and reflection-symmetry used instead. Additionally, the input-parameters for the SymPy part are converted to rational numbers where possible to speed up the calculation process (see also 5).

Once n and \mathbf{k} for each refracted ray is known, the set of homogeneous linear equations according to Eq. 4 is constructed and solved via singular value decomposition of the matrix-part which can be conveniently done in NumPy. Since each transmitted (or reflected) beam belongs to one of two possible eigenstates, we can expect that there is at least one zero singular-value with a corresponding singular-vector \mathbf{E}_i ($i = (\text{tf}, \text{ts}, \text{rf}, \text{rs})$) that marks the desired solution (only for degenerated n , two solutions will be produced corresponding to the S- and P-polarization states with respect to the intercept). From the eigenstates of the electric-field directions and the \mathbf{k} -vectors, we can derive the magnetic-field eigenstates and further the Poynting vectors which are generally not parallel to \mathbf{k} . The actual transmitted field in each eigenstate is calculated according to Eq. 7.

In general, this procedure needs to be done three times if we want to trace a beam going through the sample: for the incoming beam and for each fast/slow beam exiting the sample (see also Figure 3). For the exiting beams, however, the refraction indexes as well as \mathbf{k} are given and do not need to be calculated. In reflection, we can further assume symmetry with the eigenstates already calculated. Thus, a convenient simplification can be made. Once the exiting ray's fields are determined (there will be two), their phase-shift with respect to each other needs to be calculated. This can be done by deriving the optical-path length (OPL), given by

$$OPL_i = n_i l_i \cdot (\hat{\mathbf{k}}_i \cdot \hat{\mathbf{S}}_i), \tag{10}$$

where l_i is the path-length of the energy-flux inside the sample which is defined by S_i and the sample's thickness. Both exiting rays are generally separated and a direct superposition is thus not applicable. However, a light-field in form of a laser, for instance, possesses a certain diameter which can be imagined as a manifold of parallel rays entering the sample. An existing ray of the, e.g. fast-mode will thus superpose with another ray's exiting slow-mode which leads to a change in the ray's polarization if both superposing fields are different in direction. In addition to the OPL, another phase-shift ϕ needs to be taken into account arriving from the initial separation of the two rays from which fast and slow mode will overlap upon exiting. This phase-shift may be calculated via

$$\phi = (l_{\text{ts}} \hat{\mathbf{S}}_{\text{ts}} - l_{\text{tf}} \hat{\mathbf{S}}_{\text{tf}}) \cdot \hat{\mathbf{S}}_{\text{inc}} \tag{11}$$

and used for either the fast ray or the slow ray exiting the sample.

Overview of the Calculation Process

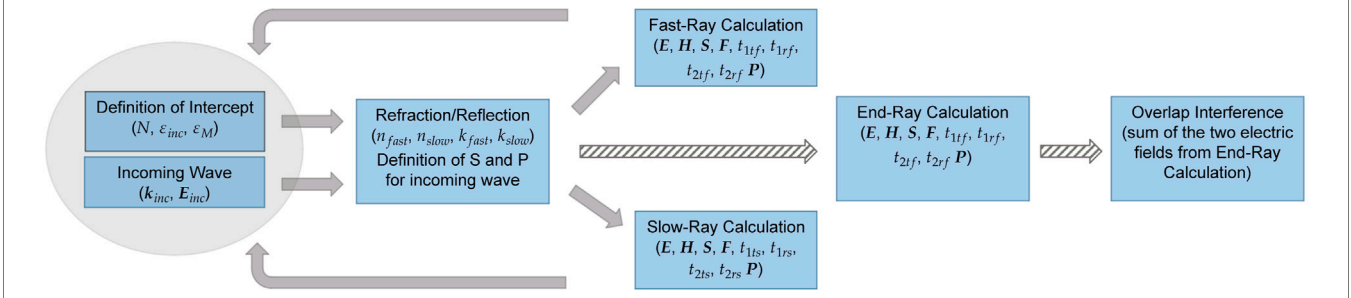


FIGURE 3 | Process chart of the code-implementation. From the two initial settings of input-ray and intercept, the refraction indexes and wavevectors of refracted and reflected rays are calculated. The derivation of the field-vectors is separately done for the fast and slow solution and serves as input for the exit-intercept (for details regarding F , please refer to the **Supplementary Appendix**). From both fast and slow solution after the exit-intercept, the field-vectors are calculated (“end-ray calculation”) and their overlap interference determined.

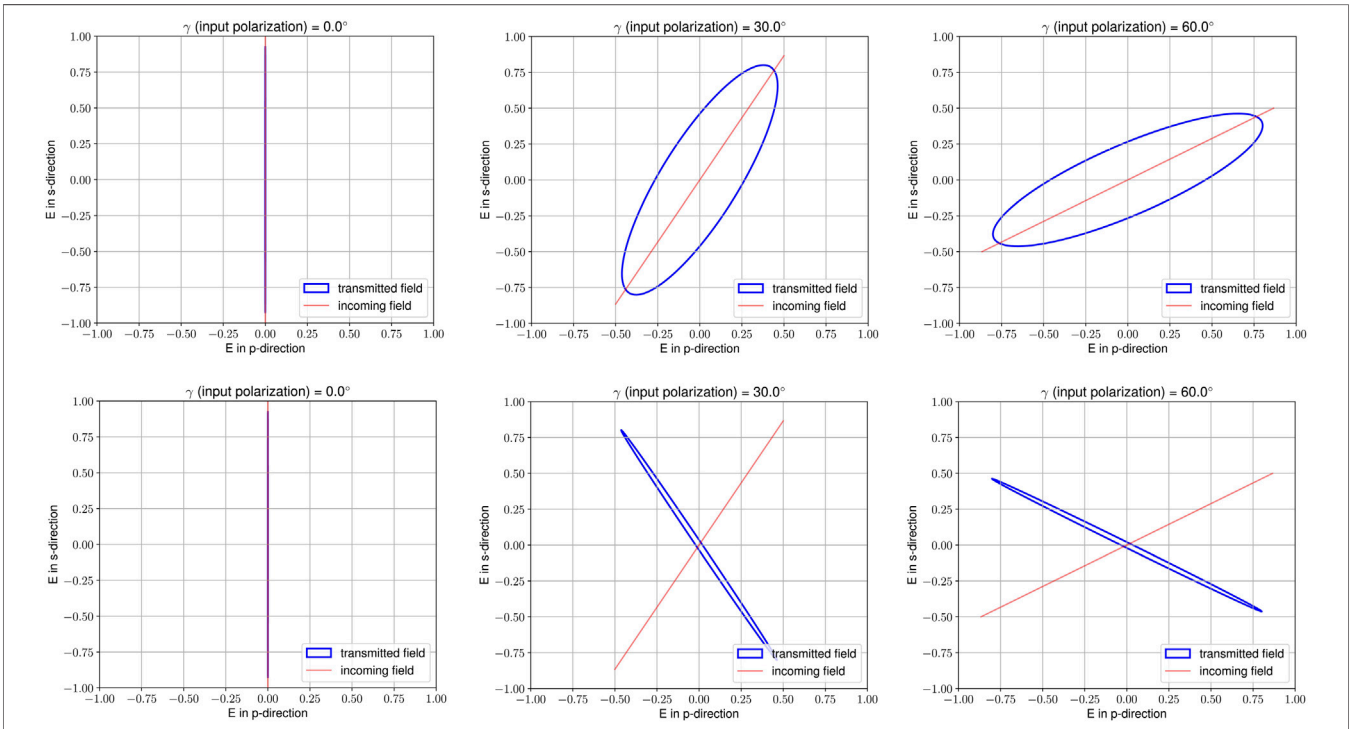
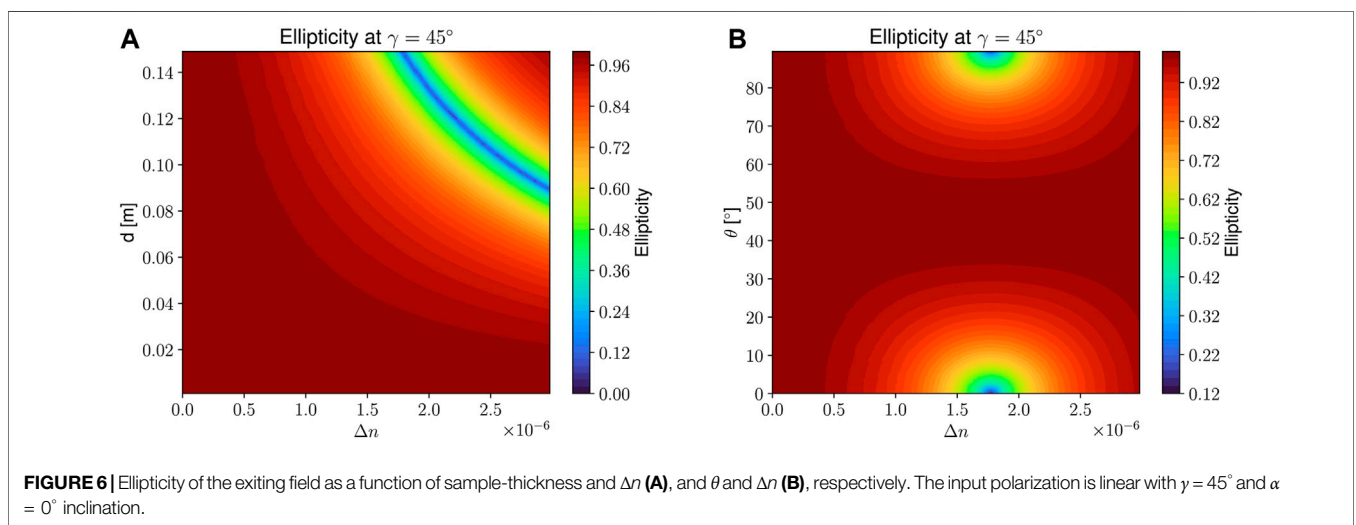
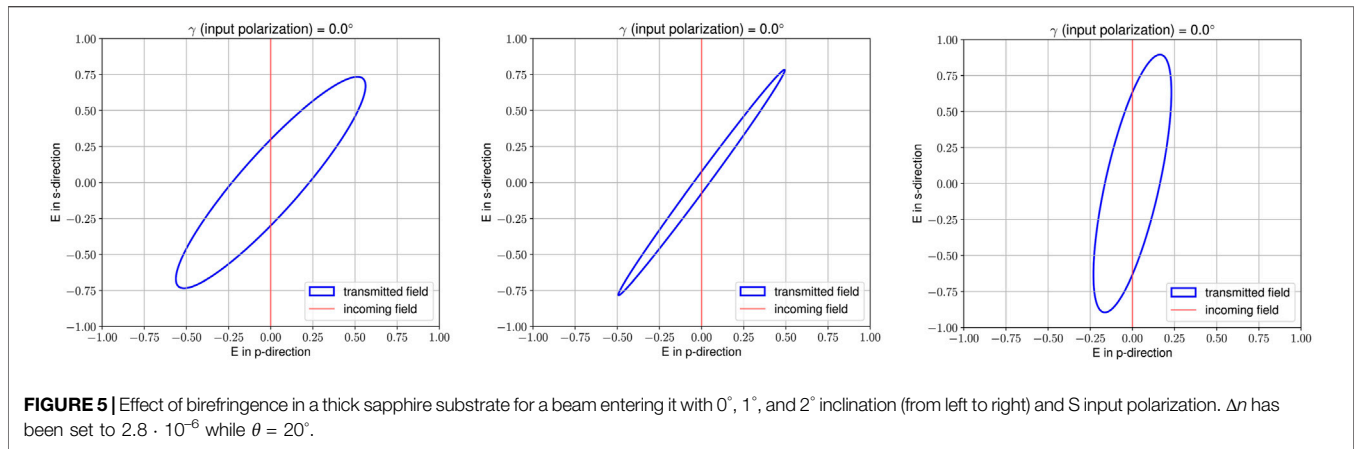


FIGURE 4 | Effect of birefringence in a thick sapphire substrate for a beam entering it with 1° inclination and varying input polarization ($\gamma = 0^\circ, 30^\circ, 60^\circ$). In the top row, the effect for $\Delta n = 0$ is given while the bottom row shows the effect for $\Delta n = 2.8 \cdot 10^{-6}$ (refer to **Eq. 9**).

3 APPLICATION OF THE NUMERICAL TOOL FOR LARGE SUBSTRATES

If we are going to analyze the polarization effects of birefringent sapphire samples, we would need an adequate way to present the results from the mere ray-trace. A possible solution can be a time-tracing of the resulting electric-field vector. The basic output of

such a time-trace can be depicted from **Figure 4**, where a ray having an inclination of $\alpha = 1^\circ$ in the x - y -plane is inserted into a sapphire sample having a thickness of 0.15 m with three different (linear) polarization directions ($\gamma = 0^\circ$ (S-polarized), 30° , and 60°), in case of $\Delta n = 0$ and $\Delta n = 2.8 \cdot 10^{-6}$, respectively. In both cases, an otherwise perfect crystal is given with axes orientation according to the left sketch in **Figure 2** and $\theta = 0^\circ$. The tips of the exiting



superposed field-vector as well as the incoming field-vector are subsequently drawn for a full 2π -cycle in the time-domain, whereas the two exiting fields are described with

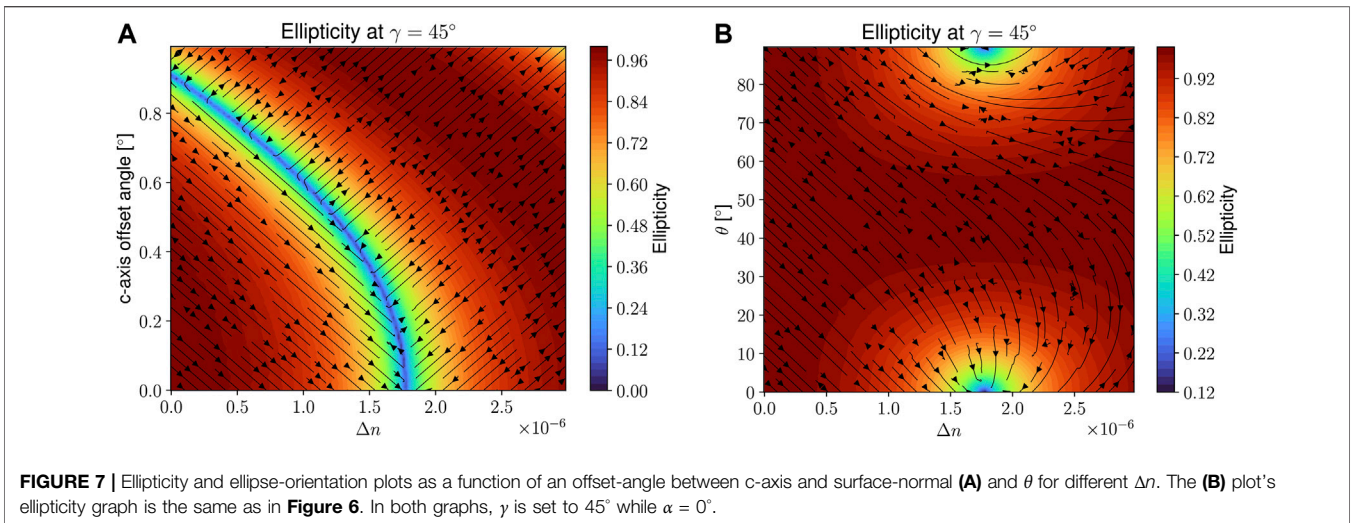
$$E_{\text{exit},i}(t) = \Re \left\{ |E_{\text{inc}}| \cdot E_{\text{exit},i} \cdot \exp \left[j \frac{2\pi}{\lambda} \cdot OPL_i \right] \cdot \exp [j2\pi\omega t + j\phi] \right\}. \quad (12)$$

Here, ϕ from Eq. 11 is used only for $i = \text{ts}$.

Unsurprisingly, a S-polarized beam will not experience any change by passing the substrate, regardless the birefringence or inclination angle as the transmitted field-component is only non-zero in x -direction which, according to Eq. 9, acts as the slow-ray due to the higher refraction index in case $\Delta n \neq 0$. For any other input polarization, however, we see non-negligible deviations. The exiting beam will become elliptically polarized whether or not Δn is zero. That is foremost the effect of the inclination angle, due to which the passing beam experiences the refraction index n_e to a certain extend even though $\Delta n = 0$. The birefringence changes the polarization in addition to the inclination, thus leading to a different ellipticity and orientation of the exiting field.

By changing the orientation of the birefringent crystal axes ($\theta \neq 0^\circ$), we see that the exiting rays become prone to polarization changes even with zero inclination (Figure 5). The effect would be thus similar to a non-zero input polarization-angle γ (note, however, that the similarity ends once the inclination becomes non-zero too). In Figure 5, example figures for $\Delta n = 2.8 \cdot 10^{-6}$ at inclinations 0° , 1° , and 2° are shown for $\gamma = 0^\circ$ and $\theta = 20^\circ$. In all three cases, the linear polarization from the input-beam changes to an elliptic polarization after exiting.

All above examples have been calculated for a sample with thickness of 0.15 m, typical for a KAGRA ITM (Akutsu et al. (2019); Aso et al. (2013)). With such thicknesses, even a small birefringence as of the order 10^{-6} (which is already in the range of mere thermal inhomogeneities) can have a severe impact on the polarization. The left graph in Figure 6 pictures the ellipticity of the exiting field as a function of thickness d and birefringence ($\theta = 0^\circ$, $\gamma = 45^\circ$). We can clearly observe a gradual decrease towards both increasing d and Δn , reaching 0 (circular polarized) for $d \approx 9$ cm and $\Delta n = 3 \cdot 10^{-6}$ and subsequently increasing again (by flipping orientation of the ellipse). The right graph in the same figure shows the effect of a changing θ -angle with $d = 0.15$ m.



As can be observed from Figures 5, 6, an important parameter for the question whether or not polarization-changes occur is the orientation of the birefringence and hence the θ -angle (or, more generally, the ϵ -tensor). As will be presented in an upcoming paper, measurements with a polariscope on spare ITMs show a θ -angle distribution ranging from $3 \sim 88^\circ$. Hence, it can be assumed that the ellipticity-map in Figure 6 presents a realistic image of the distribution of ellipticity in any of such large substrates.

Another important parameter is the orientation of the c-axis inside the crystal. Up to this point, the c-axis has been assumed to be normal to the (non-wedged) input intercept. It is however exactly this parameter which is hard to control in large sapphire substrates. Accuracy margins given by manufacturers are typically of the order 0.5° . Within this order the ellipticity can change over more than a cycle (from 1 to 0 and back to 1) even though $\Delta n = 0$, as can be observed from Figure 7. Additionally, in this figure, the orientation of the ellipse is given as an overlying stream-line plot. As already mentioned, the minimum across the graph marks the turning-point where the exiting field's polarization becomes perpendicular to the incoming field. In the same figure on the right-side, the ellipticity-plot for varying θ as from Figure 6 is shown again but together with the respective stream-line plot of the orientation.

4 IMPACTS ON GRAVITATIONAL-WAVE DETECTORS

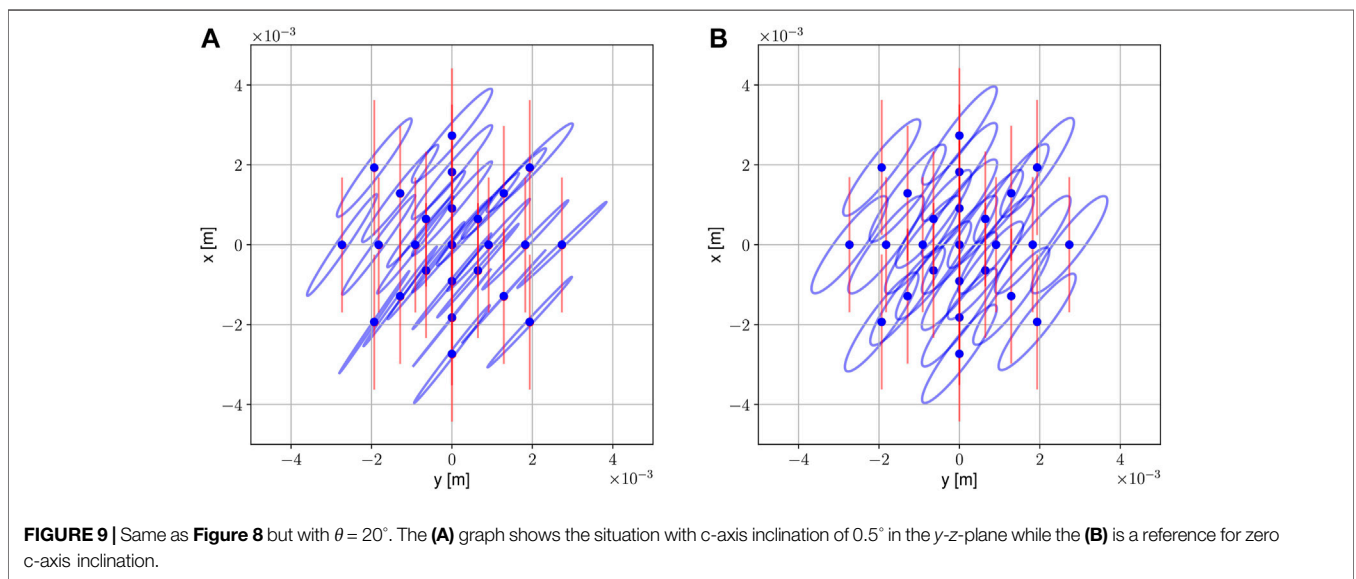
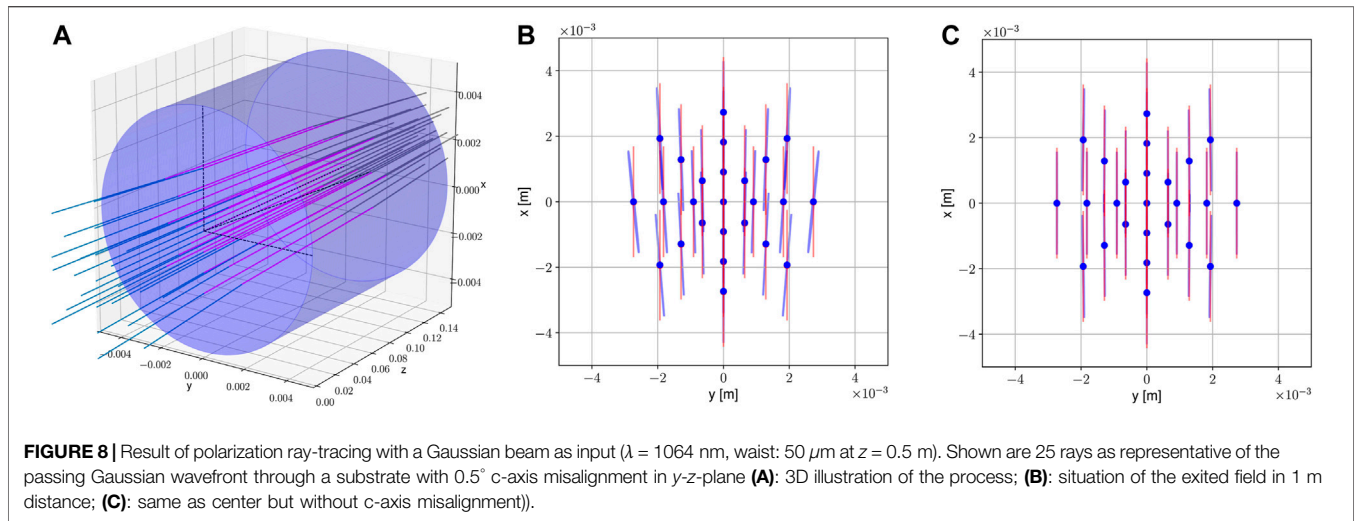
In the preceding section, the principal effects on the polarization of a transmitted beam through thick sapphire crystals have been presented. The most obvious observation up to this point is the non-negligible influence of even slight distortions in the crystal properties on the resulting electric-field. The main question for gravitational-wave detectors, however, is how much do these effects impact the sensitivity using a realistic ITM model.

Any change of the desired polarization will in principle affect the power that cycles inside the cavities due to coating design of

the mirrors. That eventually leads to contrast losses at the detector-port due to imperfections in the interference fringes. The dependence of these imperfections on Δn can be estimated after Winkler et al. (1991) to

$$\frac{P_{\min}}{P_{\max}} \approx 10^{-3} \cdot \left(\frac{d\Delta n}{\lambda/100} \right)^2, \tag{13}$$

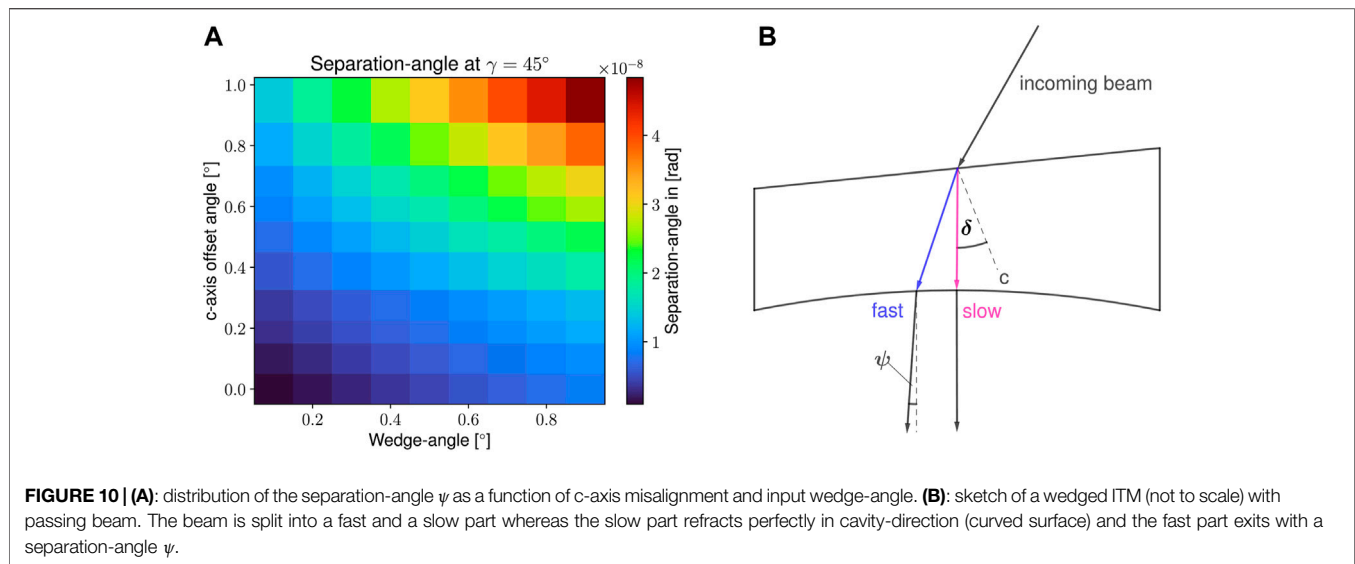
where P_{\min} and P_{\max} are the power of the dark- and the bright-port, respectively, and d the ITM thickness. Given the constraints for KAGRA (contrast: $\sim 99\%$), Δn is required to be of the order 10^{-7} or less (Tokunari et al. (2010)) which currently appears to be difficult to achieve (Dobrovinskaya et al. (2009)). It is, however, not the birefringence-value itself but rather its variance and different orientation (θ -angle) over the entire sample that is problematic. A constant value may be addressed by a proper design and orientation of the sample but without this possibility, polarization may vary within the wavefront passing through the substrate. This is illustrated in Figure 8 where the results of a simulation given a set of 25 collimated rays representing the path of a Gaussian wavefront are presented. The graph in the center shows the situation 1m after the sample in case the c-axis bears an offset of 0.5° . The dots represent the position of each ray while the red-line indicates the initial polarization-direction and the blue ellipse the exiting field. Using a birefringence of $\Delta n = 2.8 \cdot 10^{-6}$, the ellipticity is close to 1, which is expected according to Figure 7, but at the same time we observe an orientation misalignment particular for outer rays. The maximum misalignment towards the input polarization is $\sim 4.1^\circ$ meaning that almost 9% of the incoming field changes its polarization. For comparison, the situation without c-axis misalignment is given in the right graph. Please note that all graphs in Figure 8 have been calculated assuming $\theta = 0^\circ$ with the incoming field aligned. Hence, any additional influence from θ is neglected. If we add a rotation of ϵ with $\theta = 20^\circ$, we arrive at a situation as given in Figure 9, where we observe a change in polarization throughout the whole set of rays. Again, the left graph pictures the situation with c-axis misaligned in the y - z -plane and therefore shows a non-symmetric



effect. These simulations have been performed with an assumed beam-waist of $50 \mu\text{m}$ at $z = 0.5$ m for a $\lambda = 1064$ nm laser and are therefore extremely exaggerated (beam divergence here *vs.* KAGRA $\approx 258/1$). That does not change, however, the principle effects to be expected.

Up to this point, three different aspects influencing a beam’s polarization have been discussed: the expectation on Δn , the variance in θ , and the misalignment of the c-axis. Another important point, however, is the non-parallelism of the input and output surfaces, where “input” means facing the beam-splitter in a laser-interferometer and “output” means facing the cavity. The input surface possesses a wedge ($\sim 0.025^\circ$ for ITM in case of KAGRA (Akutsu et al. (2020))) to reduce the coupling with scattered light (Aso et al. (2014); Tokunari et al. (2010)), while the output-surface is curved with a radius of 1900 m (Akutsu et al. (2020)) to mimic the shape of the wavefront reflecting into the cavity (see sketch in

Figure 10). For a non-birefringent sapphire substrate ($\Delta n = 0$), the ray-splitting effect from the wedged surface given a misalignment of the c-axis in the plane of incidence can be determined analytically, as pointed out by Tokunari et al. (2010). Using the numerical tool presented in this paper, we can indeed get similar results as presented in their paper regarding internal ray-splitting (see the graph in **Figure 10**). For a purely S-polarized wave with respect to the input-wedge, ray-splitting doesn’t matter as long as $\Delta n = 0$ and c-axis misalignment is in the plane of incidence, since the refracted fast-ray will not gain any power. But, as pointed out above, both cannot be guaranteed for any sapphire substrate and either an input polarization $\gamma \neq 0$ or $\theta \neq 0$ needs to be assumed to get the results of Tokunari et al. (2010). It should be noted that a similar calculation-run by the presented numerical tool with an arbitrary c-axis misalignment changes the results as given in **Figure 10** only negligibly.



5 CONCLUSION

In this paper, a numerical tool has been presented for polarization-sensitive ray-tracing inside large birefringent media used in current gravitational-wave detectors like KAGRA. The tool is completely written in Python (version 3.8) and can be thus easily applied on any modern PC. While its main scope is the utilization in research and development for the construction of gravitational-wave detectors, the code is general enough to work for any other application in science or education. As indicated in the previous section, the code generates results which are comparable with those calculated analytically (if applicable) and hence can be used with confidence. Current limitations, however, appear wherever the numerical implementation becomes difficult. That is particular the case for problems where a precise floating-point representation of parameter values does not exist whereas precision is of utmost importance. In such cases, numerical errors appear which affect the result. Since the SymPy-solver relies on the correct transcription between floating-point numbers and its symbolic algebra, also fake-solutions or simply no solutions at all are likely to happen. Applying its internal cross-check algorithm helps in most cases but can become extremely time-consuming for solutions of n requiring precision beyond the ppm scale. Currently, there is a plan to involve other symbolic languages like “SAGE” or “symengine” for which Python-wrappers exist but meanwhile only SymPy is used for this task. The use of floating-point numbers does also lead to numerical errors which appears through their limiting accuracy. In basically all calculation steps double-float numbers (64 Bit) are used for which a limiting accuracy (round-error) of $>1.1 \cdot 10^{-16}$ can be found. In this study, a more conservative approach is being utilized and the general accuracy estimated to be $1 \cdot 10^{-14}$. The most crucial effect of this limitation can be expected from the refractive indexes and the field-vectors, which basically determine all other parameters. The exact impact of the accuracy limitation on the main results like ellipticity of the exiting field or its directional misalignment

relative to the input field depends on the specific problem, but can be estimated to be $<4 \cdot 10^{-11}$ for ellipticity and $<3.5 \cdot 10^{-11}$ for the misalignment (in radians).

For gravitational-wave detectors like LIGO, Virgo or KAGRA, the here presented tool can in any case support the evaluation of polarization effects and hence could give insights in how the sensitivity will develop when in operation, which may thus help understanding possible issues in the beam reflected from the cavities. As of now, however, the impact of a laser beam with inhomogeneous polarization on the sensitivity of the detector is a matter of ongoing investigation and cannot be discussed in details here. In KAGRA, particularly, the utilization of sapphire is a core-feature due its remarkable thermal properties at low temperatures. On the other side, we see the difficulties in sapphire’s optical behavior as birefringent crystal when assuming realistic conditions. The large thickness of ITMs is a key-aspect in this regard but not the only one. In fact, given the beam-radius at an ITM in KAGRA (~ 35 mm), we could minimize polarization effects if the substrate is chosen so that the most homogeneous distribution in Δn and θ is in its center, and that θ is aligned with the incoming polarization. That, however, requires knowledge on both Δn and θ in advance which is currently not measured as standard. A forthcoming paper on this problem is currently being written and expected to be published in the near future.

KAGRA has been chosen in this work as a prime example since it uses sapphire as TM material which is inherently birefringent and prone to affect the polarization of transmitting light. However, as mentioned in the introduction, even optical isotropic materials like silica can become anisotropic if internal stress resides which is likely the case given its manufacturing procedure. We can expect, however, that the stress is one order of magnitude smaller than for sapphire (evaluated from own unpublished data) so that the issue may not be urgent for LIGO or Virgo. With the dawn of the next generation gravitational-wave detectors like Einstein-Telescope or Cosmic-Explorer, however, the optical properties of mirror

substrates will become an issue for which research in improving the material's properties is mandatory, and for which this work is supposed to contribute.

DATA AVAILABILITY STATEMENT

The original contributions presented in the study are included in the article/**Supplementary Materials**, further inquiries can be directed to the corresponding author.

REFERENCES

- Aasi, J., Abbott, B. P., Abbott, R., Abbott, T., Abernathy, M. R., and Ackley, K. The LIGO Scientific Collaboration (2015). Advanced LIGO. *Class. Quantum Gravity* 32, 074001. doi:10.1088/0264-9381/32/7/074001
- Abbott, B. P., Abbott, R., Abbott, T. D., Abernathy, M. R., Acernese, F., Ackley, K., et al. (2016). Observation of Gravitational Waves from a Binary Black Hole Merger. *Phys. Rev. Lett.* 116, 061102. doi:10.1103/PhysRevLett.116.061102
- Acernese, F., Agathos, M., Agatsuma, K., Aisa, D., Allemandou, N., Allocca, A., et al. (2015). Advanced Virgo: a Second-Generation Interferometric Gravitational Wave Detector. *Class. Quantum Gravity* 32.
- Akutsu, T., Ando, M., Arai, K., Arai, Y., Araki, S., Araya, A., et al. (2019). Kagra: 2.5 Generation Interferometric Gravitational Wave Detector. *Nat. Astron* 3, 35–40. doi:10.1038/s41550-018-0658-y
- Akutsu, T., Ando, M., Arai, K., Arai, Y., Araki, S., Araya, A., et al. (2020). Overview of Kagra: Detector Design and Construction History. *Prog. Theor. Exp. Phys.* 2021, 05A101. doi:10.1093/ptep/ptaa125.05A101
- Aso, Y., Michimura, Y., Somiya, K., Ando, M., Miyakawa, O., Sekiguchi, T., et al. (2013). Interferometer Design of the Kagra Gravitational Wave Detector. *Phys. Rev. D.* 88, 043007. doi:10.1103/physrevd.88.043007
- Aso, Y., Michimura, Y., and Somiya, K. (2014). KAGRA Main Interferometer Design Document. *Tech. Rep.*
- Bailes, M., Berger, B. K., Brady, P. R., Branchesi, M., Danzmann, K., Evans, M., et al. (2021). Gravitational-wave Physics and Astronomy in the 2020s and 2030s. *Nat. Rev. Phys.* 3, 344–366. doi:10.1038/s42254-021-00303-8
- Bradley, D. L. (1963). *Photoelastic Constants of Synthetic Sapphire*. Master's thesis (East Lansing, Michigan: Michigan State University).
- Chipman, R. A., Lam, W.-S. T., and Young, G. (2018). *Polarized Light and Optical Systems*. Boca Raton, Florida, USA: CRC Press.
- Dobrovinskaya, E. R., Lytvynov, L. A., and Valerian, P. (2009). *Sapphire - Material, Manufacturing, Applications*. Berlin, Germany: Springer.
- Harris, D. C., Johnson, L. F., Cambrea, L., Baldwin, L., Baronowski, M., Zelmon, D. E., et al. (2017). Refractive Index of Infrared-Transparent Polycrystalline Alumina. *Opt. Eng.* 56, 077103. doi:10.1117/1.oe.56.7.077103
- Iwaki, T., and Koizumi, T. (1989). Stress-optic Law in a Single Crystal and its Application to Photo-Anisotropic Elasticity. *Exp. Mech.* 29, 295–299. doi:10.1007/BF02321411

AUTHOR CONTRIBUTIONS

SZ: Writing code, doing the analysis and writing the paper.

SUPPLEMENTARY MATERIAL

The Supplementary Material for this article can be found online at: <https://www.frontiersin.org/articles/10.3389/fspas.2022.881348/full#supplementary-material>

- Kalogera, V., Sathyaprakash, B., Bailes, M., Bizouard, M.-A., Buonanno, A., Burrows, A., et al. (2021). The Next Generation Global Gravitational Wave Observatory: The Science Book. *arXiv Prepr. arXiv:2111.06990*.
- Martynov, D. V., Hall, E. D., Abbott, B. P., Abbott, R., Abbott, T. D., Adams, C., et al. (2016). The Sensitivity of the Advanced Ligo Detectors at the Beginning of Gravitational Wave Astronomy. *Phys. Rev. D.* 93, 112004. doi:10.1103/PhysRevD.93.112004
- Nye, J. F. (1985). *Physical Properties of Crystals: Their Representation by Tensors and Matrices*. Oxford, UK: Oxford University Press.
- P. R. Saulson (Editor) (1994). *Fundamentals of Interferometric Gravitational Wave Detectors*. 1 edn (Singapore: World Scientific).
- Tokunari, M., Saito, T., Miyoki, S., Ohashi, M., and Kuroda, K. (2010). Optical Properties Measurement of an Al₂O₃ Mirror Substrate for the Large-Scale Cryogenic Gravitational Wave Telescope (LCGT). *Cl. Quantum Grav.* 27, 185015. doi:10.1088/0264-9381/27/18/185015
- Winkler, W., Danzmann, K., Rüdiger, A., and Schilling, R. (1991). Heating by Optical Absorption and the Performance of Interferometric Gravitational-Wave Detectors. *Phys. Rev. A* 44, 7022–7036. doi:10.1103/physreva.44.7022
- Zeidler, S., Posch, T., and Mutschke, H. (2013). Optical Constants of Refractory Oxides at High Temperatures. *Astronomy Astrophysics* 553, A81. doi:10.1051/0004-6361/201220459

Conflict of Interest: The author declares that the research was conducted in the absence of any commercial or financial relationships that could be construed as a potential conflict of interest.

Publisher's Note: All claims expressed in this article are solely those of the authors and do not necessarily represent those of their affiliated organizations, or those of the publisher, the editors and the reviewers. Any product that may be evaluated in this article, or claim that may be made by its manufacturer, is not guaranteed or endorsed by the publisher.

Copyright © 2022 Zeidler. This is an open-access article distributed under the terms of the Creative Commons Attribution License (CC BY). The use, distribution or reproduction in other forums is permitted, provided the original author(s) and the copyright owner(s) are credited and that the original publication in this journal is cited, in accordance with accepted academic practice. No use, distribution or reproduction is permitted which does not comply with these terms.